AFRL-RI-RS-TR-2023-095

ACTIVE PLASMONIC ANTENNA ARRAYS FOR TERAHERTZ FREQUENCY COMMUNICATIONS

RESEARCH FOUNDATION FOR THE STATE UNIVERSITY OF NEW YORK SPONSORED PROJECTS SERVICES

MAY 2023

FINAL TECHNICAL REPORT

APPROVED FOR PUBLIC RELEASE; DISTRIBUTION UNLIMITED

STINFO COPY

AIR FORCE RESEARCH LABORATORY
INFORMATION DIRECTORATE

■ **AIR FORCE MATERIEL COMMAND** ■ **UNITED STATES AIR FORCE** ■ **ROME, NY 13441**

NOTICE AND SIGNATURE PAGE

Using Government drawings, specifications, or other data included in this document for any purpose other than Government procurement does not in any way obligate the U.S. Government. The fact that the Government formulated or supplied the drawings, specifications, or other data does not license the holder or any other person or corporation; or convey any rights or permission to manufacture, use, or sell any patented invention that may relate to them.

This report is the result of contracted fundamental research deemed exempt from public affairs security and policy review in accordance with SAF/AQR memorandum dated 10 Dec 08 and AFRL/CA policy clarification memorandum dated 16 Jan 09. This report is available to the general public, including foreign nations. Copies may be obtained from the Defense Technical Information Center (DTIC) (http://www.dtic.mil).

AFRL-RI-RS-TR-2023-095 HAS BEEN REVIEWED AND IS APPROVED FOR PUBLICATION IN ACCORDANCE WITH ASSIGNED DISTRIBUTION STATEMENT.

FOR THE CHIEF ENGINEER:

/ S /
PETER A. RICCI, JR.
Work Unit Manager

/ S /
GREGORY J. HADYNSKI
Assistant Technical Advisor
Computing &Communications Division
Information Directorate

This report is published in the interest of scientific and technical information exchange, and its publication does not constitute the Government's approval or disapproval of its ideas or findings.

REPORT DOCUMENTATION PAGE

1. REPORT DATE	2. REPORT TYPE	3. DATES COVERED	
		START DATE	END DATE
MAY 2023	FINAL TECHNICAL REPORT	DECEMBER 2019	DECEMBER 2022

4. TITLE AND SUBTITLE

ACTIVE PLASMONIC ANTENNA ARRAYS FOR TERAHERTZ FREQUENCY COMMUNICATIONS

5a. CONTRACT NUMBER	5b. GRANT NUMBER	5c. PROGRAM ELEMENT NUMBER
N/A	FA8750-20-1-0500	62788F
5d. PROJECT NUMBER	**5e. TASK NUMBER**	**5f. WORK UNIT NUMBER**
		R2WV

6. AUTHOR(S)

Erik Einarsson and Jonathan P. Bird

7. PERFORMING ORGANIZATION NAME(S) AND ADDRESS(ES)

Research Foundation for the State University of New York Sponsored Projects Services
520 Lee Entrance Ste 211
Amherst NY 14228-2567

8. PERFORMING ORGANIZATION REPORT NUMBER

9. SPONSORING/MONITORING AGENCY NAME(S) AND ADDRESS(ES)	10. SPONSOR/MONITOR'S ACRONYM(S)	11. SPONSOR/MONITOR'S REPORT NUMBER(S)
Air Force Research Laboratory/RITGA 525 Brooks Road Rome NY 13441-4505	AFRL/RI	AFRL-RI-RS-TR-2023-095

12. DISTRIBUTION/AVAILABILITY STATEMENT

Approved for Public Release; Distribution Unlimited. This report is the result of contracted fundamental research deemed exempt from public affairs security and policy review in accordance with SAF/AQR memorandum dated 10 Dec 08 and AFRL/CA policy clarification memorandum dated 16 Jan 09.

13. SUPPLEMENTARY NOTES

14. ABSTRACT

In this project, we developed an electronically driven plasmonic device with the potential to generate on-chip THz signals in nanoscale transistors with specific structural asymmetry. A hydrodynamic treatment shows how the transistor asymmetry supports plasma wave amplification, giving rise to pronounced negative differential conductance (NDC). We demonstrate these behaviors in high electron-mobility transistors, which exhibit NDR in accordance with their designed asymmetry. The NDC onsets once the drift velocity in the channel reaches a threshold value, triggering a sustained plasma instability. We also show how this feature can be made to persist beyond room temperature (to at least 75 °C). We also introduced two metal-graphene hybrid reflectarray designs, one offering full beamsteering capabilities but with challenging materials requirements, and a second with more lax requirements that offers limited beamsteering capabilities. We fabricated reflectarrays based on the second design and demonstrated a clear response near the design frequencies of 1.25 and 1.0 THz. We also performed the first demonstration of non-specular reflection at 1.0 THz using a communications testbed. The outcomes of this project represent a significant step forward for efforts to develop active components for THz electronics, and will advance beamforming, beam steering, and tracking capabilities necessary for implementing active reflectarrays in THz links.

15. SUBJECT TERMS

Terahertz communications, plasmonics, transistors, active reflectarray, intelligent reflecting surface

16. SECURITY CLASSIFICATION OF:			17. LIMITATION OF ABSTRACT	18. NUMBER OF PAGES
a. REPORT	b. ABSTRACT	C. THIS PAGE		
U	U	U	SAR	35

19a. NAME OF RESPONSIBLE PERSON	19b. PHONE NUMBER *(Include area code)*
PETER A. RICCI, JR.	N/A

TABLE OF CONTENTS

LIST OF FIGURES

1.0 SUMMARY

Terahertz (THz)-band (0.1 to 10 THz) communication is envisioned as a key wireless technology to fulfill the demand for denser networks, higher data rates, and improved security. However, due to low power and high propagation loss, intelligent reflecting surfaces (IRSs) will be necessary to enable non-line-of-sight communication in the presence of blockage or to help a resource-limited quasi-omnidirectional transmitter direct its radiated power. Existing IRS designs at lower frequencies cannot be simply repurposed due to the lack of tunable control elements able to operate at THz frequencies, so researchers are looking to exploit novel properties of nanomaterials, such as graphene. As part of this project, we developed a hybrid graphene–metal reflectarray for THz communications. The fundamental building block of the reflectarray is designed to have high reflection efficiency (from the metal) and real-time tunability (by leveraging the properties of graphene). The proposed tuning element consisting of a graphene plasmonic waveguide that feeds a metallic patch antenna. After investigating the fabrication process and material limitations, we revised our design to have graphene bridge a gap in the stub of a metallic reflecting element. We then verified the feasibility of the design using terahertz time-domain spectroscopy (THz–TDS) and confirmed the expected non-specular reflection from the IRS using a THz communications testbed.

Terahertz plasma oscillations represent a potential path to implement ultrafast electronic devices and circuits. To explore this potential, we developed an electronically driven plasmonic device with the potential to generate on-chip THz signals that relies on a high-frequency instability in nanoscale transistors with specific structural asymmetry. A hydrodynamic treatment shows how the transistor asymmetry supports plasma wave amplification, giving rise to pronounced negative differential conductance (NDC). We demonstrate these behaviors in InGaAs high electron-mobility transistors, which exhibit NDC in accordance with their designed asymmetry. The NDC onsets once the drift velocity in the channel reaches a threshold value, triggering the initial plasma instability. We also show how this feature can be made to persist beyond room temperature (to at least 75 °C) when the gating is configured to facilitate a transition between the hydrodynamic and ballistic regimes (of electron-electron transport).

The outcomes of this project represent significant advances in terms of efforts to develop active sourcing and steering components for THz communications. The reflectarray results will advance beamforming, beam steering, and tracking capabilities necessary for implementing IRSs in THz links, while the electrically driven source has considerable potential for use as local oscillators that may be used to source high-frequency on-chip signals for future communication systems. In addition to addressing scientific and technological gaps identified in the National Institute of Standards and Technology *Future Generation Wireless Research and Development Report*, these contributions demonstrate potential to improve operational agility, in line with the Air Force Future Operating Concept.

2.0 INTRODUCTION

THz-frequency wireless communication [1, 2] is an emerging technology that extends the radio spectrum to frequencies that are largely unused and unallocated (0.1 to 10 THz). Depending on the transmission distance and channel composition, the THz band can support transmission bandwidths up to a few THz. Being the first to exploit this spectral region can provide an unmatched technological advantage. Moreover, high propagation loss at targeted frequencies can be engineered to create intrinsically secure short to medium-range communication channels. Atmospheric absorption therefore drastically limits the ability of ground-based systems to intercept or disrupt air-to-air communications, improving the security of air-to-air THz links. These factors enable secure, wireless Terabit-per-second communications, opening the door to transformative applications such as high-speed big-data sharing within *ad hoc* networks of unmanned aerial vehicles for real-time monitoring and control. Such applications have not yet been realized, primarily due to the lack of compact, high-power THz sources that operate at easily accessible temperatures. This limitation has limited the use of the THz band for any application beyond sensing.

2.1 THz Source

Plasma wave generation can occur when a dc current flowing through a device exceeds a threshold value, allowing an initial plasma excitation produced by ambient noise to be amplified after reflection from the edges of a plasmonic cavity formed under a statically biased gate [3]. This phenomenon, which occurs at THz frequencies, is known as the Dyakonov–Shur instability. In order to observe such amplification, however, the impedance at the ends of the cavity must be highly asymmetric, i.e., low at the source and high at the drain [3, 4]. While significant experimental effort has focused on implementing plasmonic THz devices, the power radiated into free space has proved to be too weak for practical use. One of the main reasons for this problem is the difficulty in creating asymmetric cavity boundaries. With the support of a grant from Air Force Office of Scientific Research (AFOSR), we implemented the active part of a HEMT channel by etching two narrow constrictions of different width in the 2D channel near the source and drain terminals, as shown in Figure 1. The left panel shows a schematic illustration of the plasmonic device. The right panel shows a false-color scanning electron micrograph of the device (above) with the constriction and gate region magnified (below). The source terminal, formed by a grounded ohmic contact, together with a wide constriction defining the boundary for plasma waves, present a near-short-circuit boundary condition for plasma excitations [3]. On the drain side, we approximate a near-open-circuit condition by etching a narrow constriction, which effectively depletes electrons close to the drain. [5]. The constrictions define terminating impedances Z_s and Z_d, with $Z_s \to 0$ and $Z_d \to \infty$. With these asymmetric boundary conditions in place, the HEMT channel is transformed into a plasmonic cavity [3, 6].

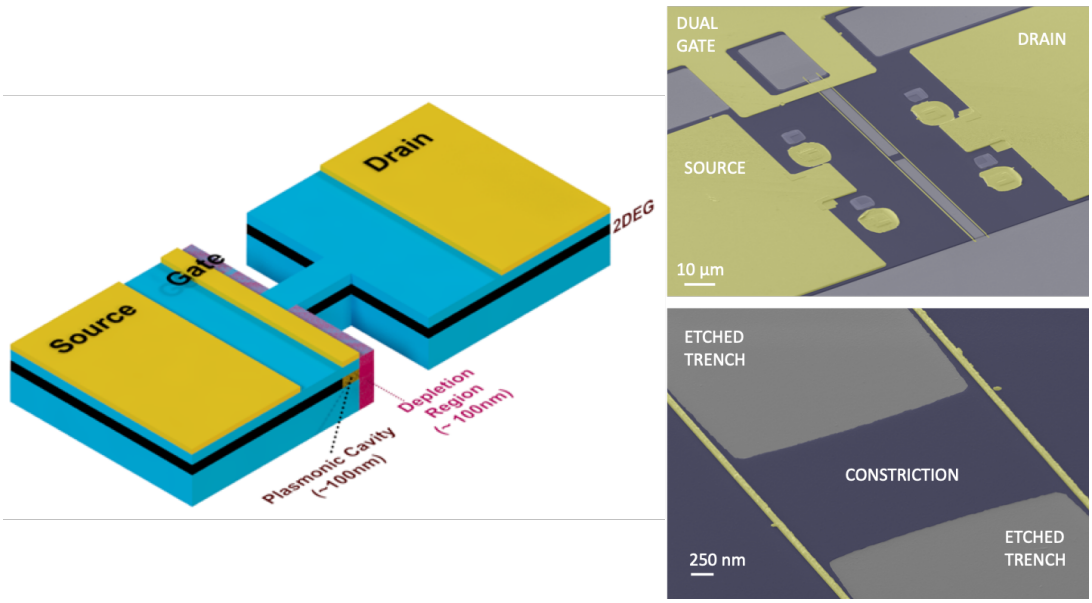

Figure 1. Illustration and Colorized Electron Micrographs of Fabricated Plasmonic Device

2.2 THz Array

In addition to a need for improved THz sources, beamforming and beam steering capabilities at THz frequencies are essential. Not only would such control facilitate transmission and detection of signals, but they are crucial for beam tracking and alternate path finding in the case of beam blockage. Overcoming significant spreading loss requires highly directional systems, enabling ultra-low probability of intercept/detection communications. There is a critical need for antenna arrays with these capabilities in the THz band.

The underlying challenge is that THz frequencies are either extremely high or extremely low, depending on the reference technology. From an electronics perspective, THz is extremely high frequency. Recent advances are pushing the limits of standard silicon complementary metal-oxide semiconductor (CMOS) technology [7], SiGe BiCMOS technology [8], III–V high electron-mobility transistor (HEMT) [9], metamorphic HEMT [10], heterojunction bipolar transistor (HBT) [11], and Schottky diode [12] technologies ever closer to the coveted 1 THz mark. From a photonics perspective, THz is very low frequency, but advances in photodiodes [13], photoconductive antennas [14], optical downconversion systems [15] and quantum cascade lasers (QCLs) [16] are bringing high-power optics down to the far infra-red and THz range. More recently, the use of nanomaterials is enabling development of novel devices for THz communications [17]. These devices are intrinsically fast, efficient at THz frequencies, and can support very large modulation bandwidths. Of particular interest is graphene, which has the ability to support surface plasmon polaritons (SPPs) at room temperature. Moreover, graphene's unique band structure facilitates electrical tuning of its conductivity.

With prior support from AFOSR, we studied electrically driven sources and graphene-based antennas for the THz band. Our results, based on simulation-informed design and fabrication, showed that all-graphene plasmonic antennas had some severe limitations, but an on-chip, electrically driven plasmonic THz source was feasible. The motivation for this project is to build upon these past results and elevate this emerging technology.

2.3 Overview of the Proposed Work

A lack of materials that can be actively tuned to operate at true THz frequencies is a major factor responsible for the challenges related to devices and research in THz communications. Graphene is arguably the most promising material for THz appilcations, and is one of the only materials known that shows the required tunability at mid-IR and THz frequencies [18, 19, 20]. Despite these attractive properties, relying solely on graphene-based plasmonic antenna arrays is not viable on a large scale. One reason is that thousands of micrometer-sized elements would need to be patterned out of a continuous monolayer, but synthesis and transfer of high-quality graphene at a sufficiently large scale remains a challenge. High reflected output power and the capability of steering the reflected beam, along with the operation at frequencies at or above 1.0 THz, are the major goals of current wireless communications research. Despite graphene's intrinsic support of THz-frequency SPPs, metallic array elements are still preferred for the designing and manufacturing of antennas due to their high reflectivity and ease of fabrication. However, all-metal antennas antennas are usually passive devices that lack variable control over a large range for angular beam steering and beamforming. An additional component must therefore be incorporated into a metallic reflectarray to provide a tuning mechanism, and we aim to provide the first demonstration of this technology.

We started from all-metal passive reflect arrays and considered how to incorporate graphene-based active control elements. In tandem with our collaborators, we then designed and simulated a hybrid array consisting of metal and graphene. The initial design consisted of metallic patches fabricated on a continuous monolayer graphene film, and the parameters used in these simulations for graphene were extracted using a THz–TDS system. Figure 2a shows THz-TDS spectra of all-metal vs graphene–metal hybrid patch antenna reflectarray. The response is clearly weaker for the hybrid array [21]. We measured no resonance behavior at the intended 1.5 THz frequency, but some enhancement in the reflection relative to the reference substrate (Si/SiO_2) for the metal only array can be clearly seen above 3.5 THz frequency. This enhancement is somewhat reduced in the case of the metal-graphene hybrid array structure. We attribute this to the conduction boundary being less pronounced, hence the electric field "leaks" out of the metal patch, as can be seen in the simulations in Figure 2b. Based on this result, we focused on exploiting graphene's tunable electrical properties while keeping the high reflectivity of metallic array elements. The goal of the proposed work is therefore to combine the high reflected output from a metallic reflectarray with the tunability of graphene by incorporating both into each individual array element.

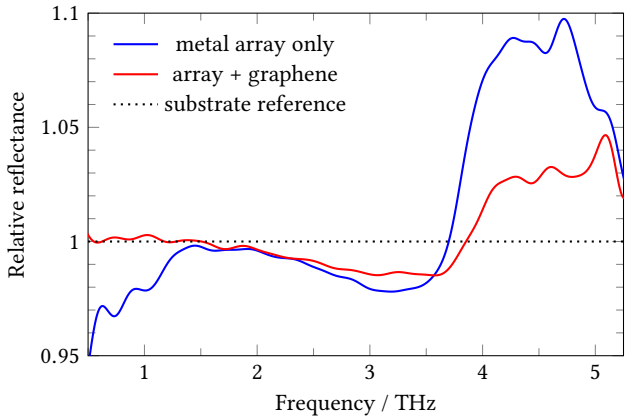

(a)

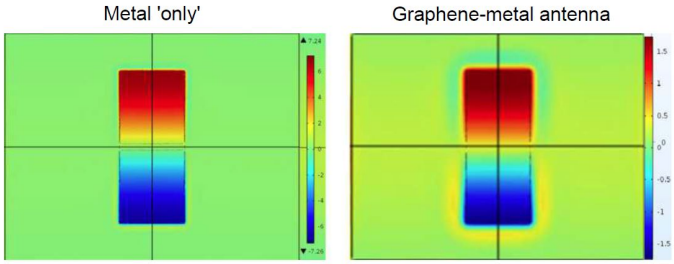

(b)

Figure 2. Measured and Simulated Response of Graphene–Metal Hybrid Antenna Array

3.0 METHODS, ASSUMPTIONS, AND PROCEDURES

3.1 Graphene Growth and Transfer

3.1.1 Cu Foil Cleaning. Before running the graphene growth procedure, the Cu foil needs to be cleaned in order to remove any impurities that are present on the surface of the foil. The as-received copper foil (25 µm thick) was cleaned by sonication in acetone and isopropyl alcohol (IPA) for 10 min each followed immediately by immersion in hydrochloric acid for 10 min to remove the native oxide layer [22] and any metal impurities from the Cu surface [23]. This was followed by sonication of the foil for 5 min in deionized (DI) water water to remove any residual acid from the Cu surface. Finally, in order to suppress graphene nucleation [24], we placed the clean Cu foil on a 300 °C hot plate for 40 min to oxidize the surface. The foil was then slowly cooled down by reducing the temperature by 250 °C every 5 min.

3.1.2 Chemical Vapor Deposition. Monolayer graphene was grown using a chemical vapor deposition (CVD) setup similar to the simplified illustration shown in Figure 3a. After the Cu foil was cleaned, it was placed at the center of a quartz tube passing through a 90 cm horizontal three-zone split furnace (Carbolite HZS 12/600). The temperature in the furnace was then raised to 1000 °C at a rate of 15 °C min^{-1}. A mixture of 5% hydrogen (H_2) in 95% nitrogen (N_2) at a

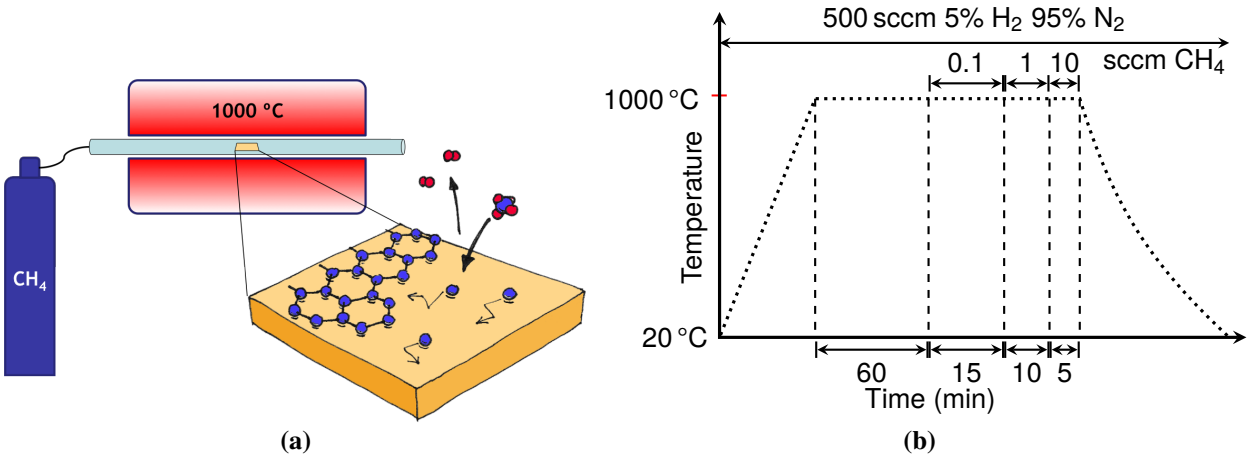

Figure 3. Illustration of Graphene Synthesis and Profile of Growth Process

flow rate of 500 sccm was continuously supplied to the reaction chamber. The Cu foil then was annealed for 60 min after the temperature in the furnace stabilized at the desired growth temperature. Polycrystalline Cu surface recrystallizes in the (100) orientation due to annealing [25]. The continuous flow of H_2 helps remove the nucleation-suppressing oxide layer from the surface to facilitate graphene growth [26]. A carbon precursor (usually methane) is then supplied to the clean Cu surface via an inert carrier gas at high temperature. These steps of the growth process are shown in Figure 3b. The heating rate was 15 °C min^{-1}. The annealing time for the Cu foil was 60 min, the CH_4 precursor was supplied for 30 min during which the flow rate was increased stepwise. At the end of 60 min Cu foil annealing process, methane (CH_4) gas (99.97% purity) was introduced in the reaction chamber in the following three steps: 0.1 sccm for 15 min, 1 sccm for 10 min, and then 10 sccm for 5 min. The supply of 5% hydrogen (H_2) in 95% nitrogen (N_2) at a flow rate of 500 sccm was continuously on during these steps (Figure 3b). A pressure of 17 Torr was maintained throughout the growth process. At the beginning of growth, the partial pressure ratio of H_2 to CH_4 was 250 in order to maximize the growth rate [27]. This was reduced in steps as growth progressed to achieve full graphene coverage. After growth, the chamber was opened for rapid cooling while maintaining the 5% H_2 flow to protect the graphene film from oxidization.

One of the drawbacks of CVD grown graphene is its polycrystalline nature. Grain boundaries can cause scattering resulting in an increase in the resistance [28]. It has been shown that the mobility in a polycrystalline CVD can be upgraded up to 90% of the single crystal graphene by having smoother or well-stitched grain boundaries [29]. Thus, increasing the overall grain size of graphene can be an important step in realizing high quality, low scattering graphene structures. Growth of large micron size single crystals of graphene have been reported by Yu et al. [28, 30]. Millimeter-scale graphene grains have also been grown using CVD [31, 32] that can be used where large mm scale sheet of graphene is required either to be patterned or used as a film.

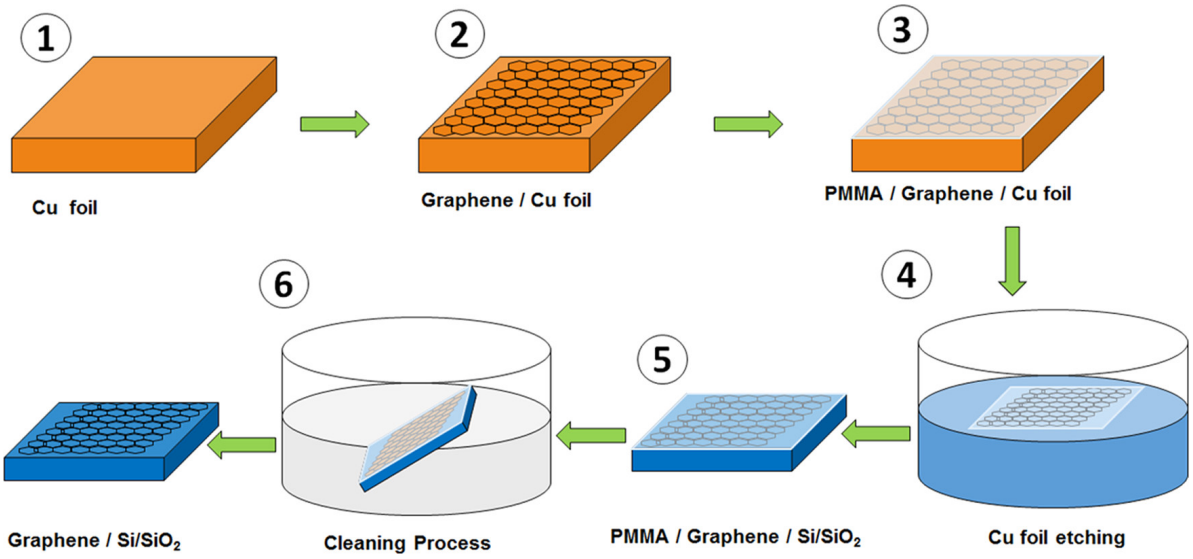

Figure 4. Graphene Wet Transfer Procedure

3.1.3 Graphene Transfer. While mechanically exfoliated graphene flake can be put on a Si/SiO_2 substrate directly from the scotch tape, graphene films grown on a Cu foil need to be transferred onto a substrate to fabricate and measure electronic devices. The wet transfer technique, such as that shown in Figure 4 [33] is most commonly used to transfer a graphene film onto a Si/SiO_2 substrate. In this method, the graphene grown on a Cu foil is spin coated with a polymer layer to provide structural stability. The Cu foil is subsequently removed through dissolution in an etchant solution, and the graphene+polymer film is 'fished' from the solution using the target substrate.

The most commonly used polymer for assisting graphene transfer onto a Si/SiO_2 substrate is polymethylmethacrylate (PMMA), which is spin coated at 3000 rpm for 45 s on the graphene monolayer grown on a Cu foil and then baked at 180 °C for 3 min. Bilayer coating of PMMA can also be done. This second layer of PMMA provides relaxation to the first PMMA layer thereby increasing continuity and reducing the occurrence of cracks in graphene [34, 35]. Recently, another PMMA-based approach showed nearly 99% continuity in monolayer graphene where instead of coating two layers of PMMA, a layer of a copolymer (MicroChem, MMA(8.5)MAA EL9) was coated on top of the PMMA layer [36].

3.2 Reflectarray Fabrication

To resolve the aforementioned issue, we fabricated the same array designs on substrates with a 300 nm (20 nm Ti + 260 nm Ag + 20 nm Au) metallic ground plane deposited on the Si/SiO_2 substrate. A 2.3 µm SU8 layer was spin coated on the deposited ground plane and the reflectarray designs were patterned on the SU8 dielectric layer by photolithography. 300 nm was chosen to ensure that the metal is sufficiently thicker than the skin depth for THz waves incident on Ag to ensure high reflectivity [37].

The fabrication steps for this reflectarray are as follows. A Si/SiO_2 substrate was cleaned by sonication in acetone, IPA, and DI water for 5 min each, followed by N_2 blow dry and heating for 5 min at 150 °C. The substrate was then treated with O_2 plasma in an inductive coupled plasma-reactive ion etching (ICP-RIE) chamber with 65 W reactive ion etching (RIE) power for 120 s. The O_2 flow rate was set to 98 sccm and the pressure in the chamber was 300 mTorr. This helps in removing organic contaminants from the surface of the substrate. The clean and contamination free substrate was then inserted into an electron beam evaporator physical vapor deposition (PVD) system at 10^{-6} Torr for the deposition of ground plane metal. The structure of the deposited metal was: 20 nm Ti, 260 nm Ag, and 20 nm Ti. Silver was chosen as the desired ground plane metal as it shows the highest reflectivity amongst all the metals. The 20 nm Ti layers on top and bottom of Ag served as adhesion layers. 0.1 µm SiO_2 was then deposited on top of the metal at 10^{-6} Torr.

To create a 2.3 µm separation layer, we chose SU8 (dielectric constant, $\kappa = 2.75$) as the dielectric material. SU8 2002 was mixed with SU8 2010 in a 5:1 ratio to get the desired viscosity. This mixture was spin-coated on the sputtered SiO_2 at 3000 rpm for 30 s followed by post-coat bake at 95 °C for 1 min. The baked SU8 was then exposed to UV light for 40 s using a mask aligner followed by a post-exposure bake at 150 °C for 4 min. This hardens the coated layer of SU8 making it adhere to the underlying SiO_2. As the adhesive strength between metal and SU8 is weak, another 0.1 µm layer of SiO_2 was deposited on top of this exposed 2.3 µm SU8 in order to ensure the adhesion. We have found that in the absence of these sputtered SiO_2 layers, the SU8 fails to stick to the ground plane and to the array and is removed during the final lift-off process.

Photolithography was used to write the array pattern onto the substrate. In order to get better lift-off results, a bilayer photoresist coating approach was used. First, LOR3B photoresist was spin coated on the substrate (Si/SiO_2 + ground plane + dielectric separation layer) at 2500 rpm for 45 s followed by post-coat bake at 190 °C for 4 min. A second photoresist (Microposit S1813) was then spin coated at 5000 rpm for 45 s on top of the LOR3B followed by post-coat bake at 115 °C for 1 min. The substrate was subsequently placed in contact with the designed photomask using the mask aligner and UV exposed (i-line, 350 W Hg lamp) for 50 s (4.5 A).

After the photolithography, the photoresists were developed in Microposit MF-319 solution for 45 s followed by rinsing in DI water for 30 s. A 300 nm layer of metal (20 nm Ti, 260 nm Ag, and 20 nm Au) was deposited to form the metal arrays. The Au layer on top was deposited in order to prevent the Ag surface from oxidation. The sample was then left in Microposit Remover 1165 solution overnight at 70 °C. After the lift-off, the sample was rinsed in IPA and DI water for 5 min each, followed by N_2 blow dry.

3.3 Array Characterization

We characterized the antenna and array response in two ways. The first is using an Advantest TAS7500TS THz–TDS (Figure 5), which has a nominal range of 0.3 to 4 THz or 0.5 to 7 THz,

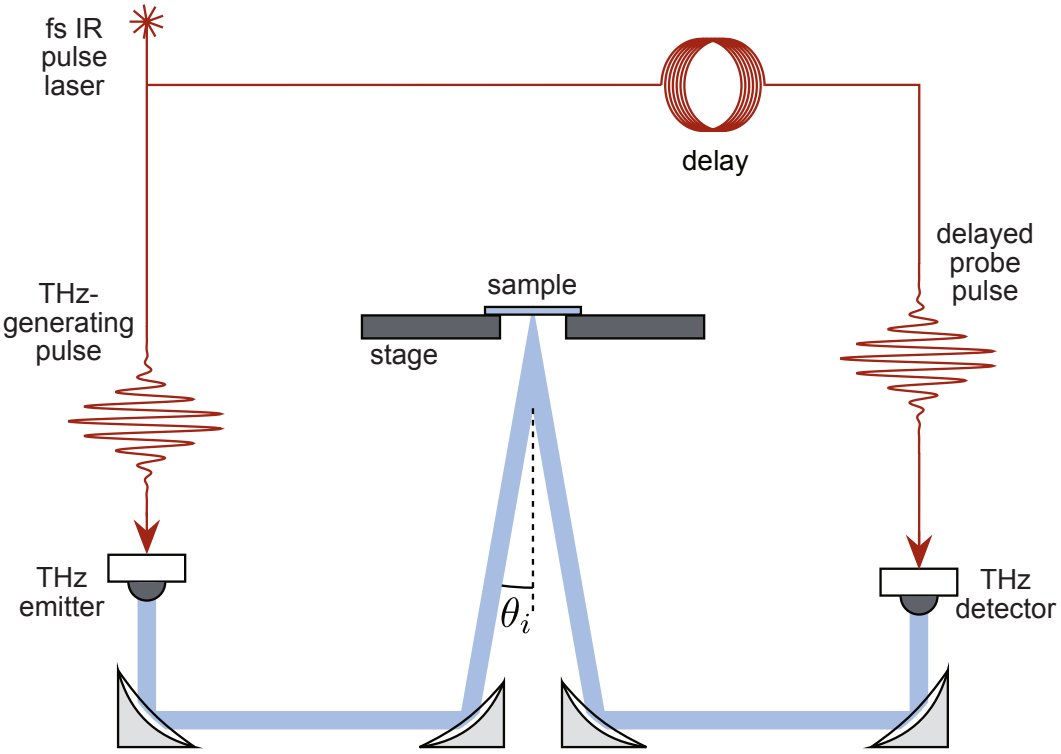

Figure 5. Schematic of the THz–TDS Measurement Setup in Reflection Geometry

depending on the emitter. The advantage of this system is rapid, broadband measurements in reflection or transmission. Acquisition of both amplitude and phase information allows direct extraction of complex permittivity, conductivity, and related optical properties. Antennas were initially designed for for 1.25 THz to match the peak sensitivity of this system, but later designed for 1.0 THz to match the fixed wavelength of the *TeraNova* platform [38], which was used to verify the design by detecting the expected non-specular reflection.

3.4 Electrically Driven THz Source

3.4.1 Heterostructure Material and its Properties. Gated transistors were fabricated in InGaAs/InAlAs heterostructures grown by molecular-beam epitaxy on InP substrates [39] . Hall measurements of ungated sections of two-dimensional electron gas (2DEG) were used to determine the electron carrier density $n \approx 2.8 \times 10^{12}\,\mathrm{cm}^{-2}$. The mobility μ (mean-free path l_{mfp}) of the 2DEG was determined to be $84\,100\,\mathrm{cm}^2\,\mathrm{V}^{-1}\,\mathrm{s}^{-1}$ (2.3 µm) at 3 K, $62\,300\,\mathrm{cm}^2\,\mathrm{V}^{-1}\,\mathrm{s}^{-1}$ (1.7 µm) at 77 K, and $13\,400\,\mathrm{cm}^2\,\mathrm{V}^{-1}\,\mathrm{s}^{-1}$ (0.4 µm) at 300 K. While l_{mfp} was therefore longer than the gate length over the entire range of temperatures studied, this should only be taken as a qualitative indicator, since this length scale pertains to low-field, single-particle transport rather than the collective plasmonic response at large drain bias. Nonetheless, the values of μ and l_{mfp} should be considered indicative of the high quality of our devices.

3.4.2 Fabrication of Transistors with Asymmetric Geometries. After first defining the device mesa, a trench was formed on the drain side of the device by electron-beam lithography and wet etching. Electron-beam lithography and lift-off was used to create the nanoscale (Ti/Au: 20/150 nm) metallic gate (~100 nm long), which was deposited over the width (~115 μm) of the 2DEG mesa. The gate was precisely aligned (within ~150 nm) with one edge of the trench. A representative device [40] is shown in Figure 6a. Figure 6b shows a schematic of the layered structure (not drawn to scale) of this material as seen along the dashed line AB in Figure 6a. Silicon delta-doping layers are inserted in the upper (8 nm) InGaAs layer, where the source and drain contacts (at ground and V_d, respectively) are formed, and in the 18 nm InAlAs spacer. An additional delta-doped layer is also present at the interface between the InGaAs and the InP etch-stop layer. The gate-defined plasmonic cavity is directly connected to a large area of 2DEG that functions as the source and which provides a relatively small (capacitive) gate-to-source ac impedance (see Figure 6b). On the other side, the extreme proximity (~150 nm) of the gate to the etched trench introduces a large gate-to-drain impedance that is essentially set by the trench width (i.e., $Z_d/Z_s \gg 1$). Although this impedance is maintained over almost the full mesa width, a conducting aperture is introduced near the center of the trench (as shown in Figure 6a). This feature is needed to enable the steady-state flow of (dc) current from source to drain, a prerequisite [3] for triggering the DS instability. As such, the plasmonic excitation is assumed to occur in the gated regions on either side of the aperture rather than in the vicinity of the aperture itself. Although we did not systematically investigate the impact of the aperture geometry on the resulting transistor characteristics, its width was chosen to be sufficiently large (~5 μm) to ensure that its contribution to the overall source-drain resistance was smaller than that of the gated region.

Fabricated devices were wire-bonded in a chip package and mounted in the light-tight vacuum enclosure of a variable temperature (3 to 500 K) cryostat. The transfer (I_d-V_g; V_d = 100 mV) and transistor (I_d-V_d) curves of the devices were measured with a Keithley 2400 dc source-measure unit. For consistency, we focus on the results obtained in a comprehensive study of a single device. We emphasize, however, that the key behaviors reported in this work were reproduced consistently in studies of numerous devices. Figure 6c shows calculated I_d–V_d curves (main panel), obtained within our model for the plasmonic instability [40]. Moving from the lowermost (black) to the uppermost (red) curve at V_d = 200 mV, the electron density in the channel is increased from 3.5×10^{11} to 1.2×10^{12} cm^{-2}, in increments of 0.5×10^{11} cm^{-2}. The four insets show the calculated time-dependent variation of the current at the source, resulting from the application of instantaneous current perturbations at the indicated values of V_d and for $n_o = 1.0 \times 10^{12}$ cm^{-2}. Sustained THz oscillations are observed when V_d = 130 mV, lying within the region of NDC (see I_d–V_d curve with solid symbols).

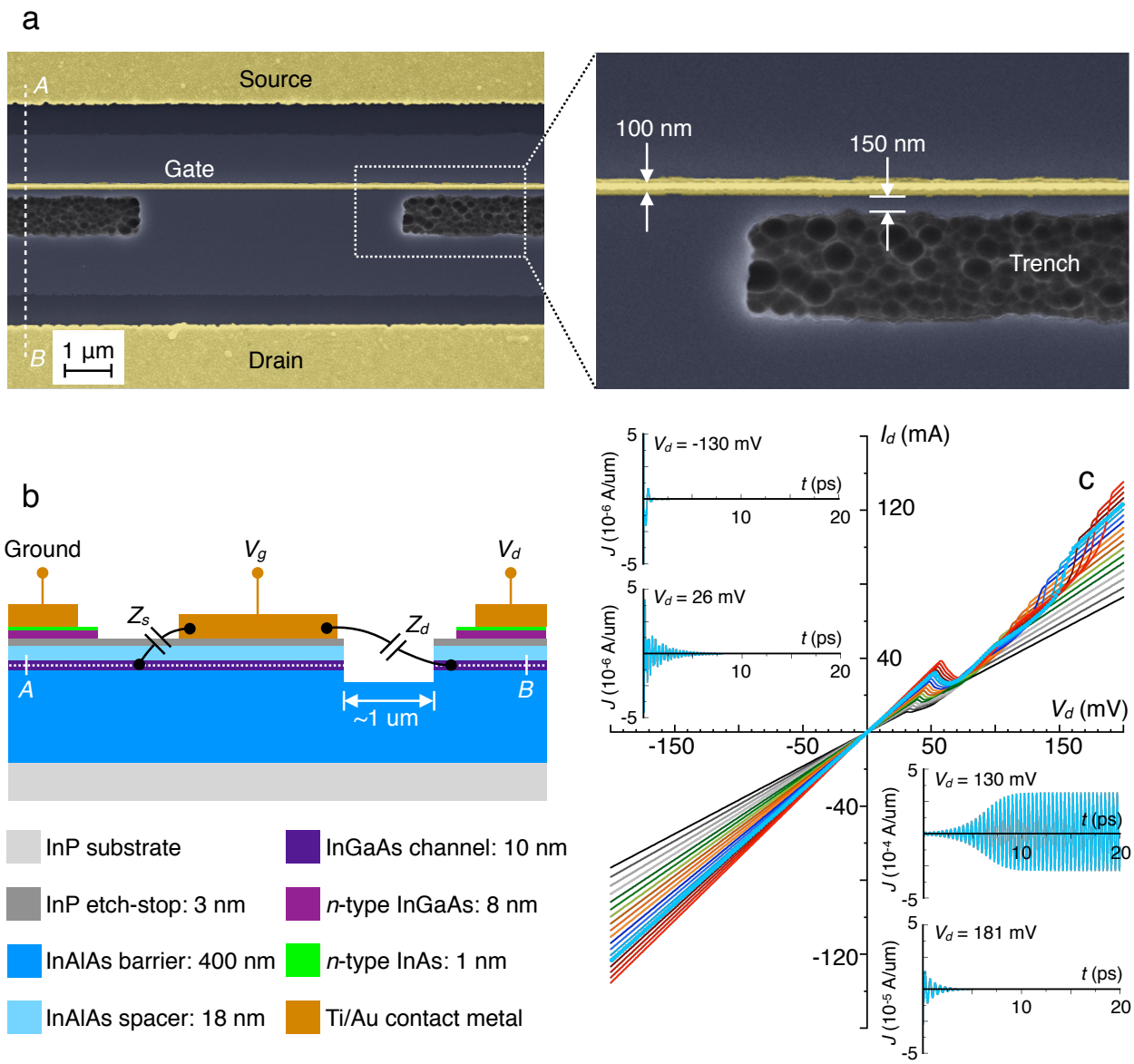

Figure 6. Fabricated 2DEG Plasmonic Cavity and Calculated Current Responses Expected for a Plasmonic Instability

4.0 RESULTS AND DISCUSSION

4.1 Electrically Driven THz Source

Initially, we explored strategies for detection of radiation emission using sensitive doped Ge bolometers, as well as using a Dyakanov–Shur field-effect transistor (FET) itself to detect radiation emitted by an identical structure (based on the idea of emitter/detector reciprocity). These measurements were ultimately inconclusive because we could not eliminate thermal heating as a possible cause for the weak detected signal.

Electrical measurements were much more informative. The current–voltage characteristics in Figure 7a show a clear asymmetry in forward and reverse bias at 3 K, with an NDC feature appearing in forward bias above a sufficiently negative gate bias. Figure 7b clearly shows this by adding a third axis for the gate voltage. For sufficiently strong gate voltage, the NDC feature we had observed at low temperature (Figure 7 upper panels) was found to persist even above room temperature (Figure 7 lower panels). Our plasmonic devices are fabricated on an InP based InGaAs/InAlAs heterostructure, in which the constriction is defined by wet etching. The significance of the boundary conditions is apparent when the current direction is reversed (thereby inverting the cavity boundary conditions). In this case, the current instability is no longer observed.

To explain the "cusp" feature observed in Figure 7, we developed a simple resistance model (Figure 8a) in which the Dyakonov–Shur FET channel acts as a resistor in series with a second resistance that depends on the current density through the channel. The onset of plasma-wave amplification is manifested in transport measurements as the opening of this second channel above a threshold voltage. This causes a small but sudden drop in the dc current through the channel, as seen in Figure 8b. Note that the applied drain bias will drop predominantly across the transistor gate under conditions where NDC is manifested because the resistance of the unetched constriction is very much smaller than that generated by the biased gate. We consider this second resistance to be radiation resistance that contributes only for current densities between two arbitrary values j_1 and j_2. These current densities correspond to applied voltages V_1 and V_2, which we set experimentally. When $j_1 \leq j \leq j_2$, the current density is given by

$$j = \frac{V}{R + \frac{A}{j^{\alpha+2}}}.$$

Starting at $V = 0$ we gradually increase voltage (horizontal axis in Figure 8b) and measure the current (vertical axis). Below V_1 there is no radiation resistance, so $R_{\text{rad}} = 0$ and we simply have the ohmic relation $V = jR$. This is represented by the diagonal dashed line. The voltage $V = V_1$ corresponds to the current density j_1 at which $R_{\text{rad}} \neq 0$, so the radiation resistance switches on. This induces a *drop* in current density, and is the negative differential conductance we observe in our experiments. As we increase V further, the current and voltage follow the parabolic relation described by the model. When $V = V_2$, the radiation resistance switches off and R_{rad} again equals

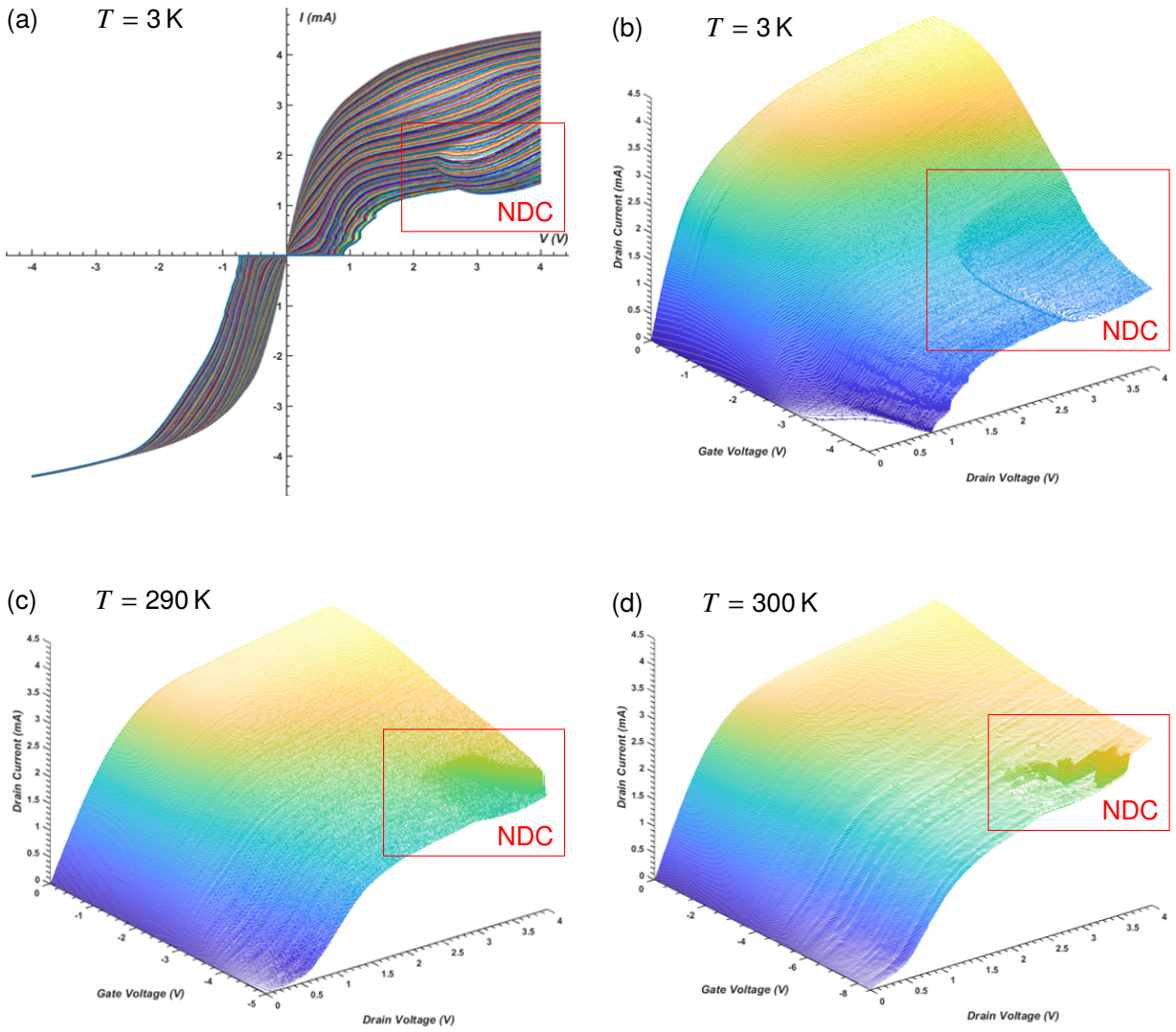

Figure 7. Measured Current–Voltage Characteristics Showing Negative Differential Conductance from Cryogenic to Room Temperature

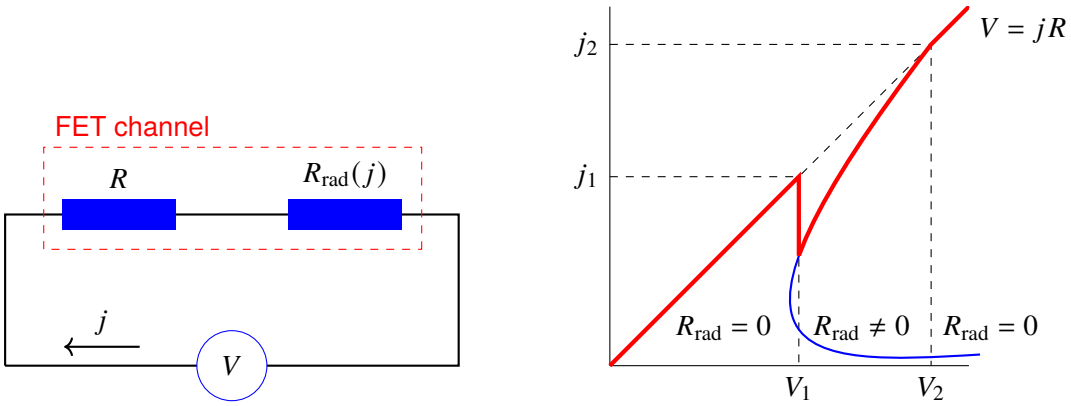

Figure 8. Simple Circuit Model and Predicted Current–Voltage Relation of FET Channel in Series with a Radiation Resistance

zero. At this point the current–voltage relation jumps back to the diagonal $V = jR$ line, but the two relations have nearly merged by this point so the size of this current jump is negligible. The observed current–voltage relation indeed follows the red line shown in Figure 8b, exhibiting NDC with an abrupt cusp at lower voltage and a smooth return at higher voltage. The parabolic relation is much more important than the exact values of fitting parameters A and α.

We spent a considerable amount of time comparing our experimental data to numerical calculations performed by our collaborators, and after examining all potential alternate explanations for our observed data we are convinced that the Dyakonov–Shur plasmonic instability is the correct explanation. While there is good qualitative agreement, the radiated power differs from the observed power loss by a few orders of magnitude. After several cycles of theory, simulation, and comparison with experiment, our conclusion is that the vast majority of power is lost via Joule heating [40]. As a THz source, this means we will need to couple to the plasma oscillation rather than radiate directly from the device. Our findings suggests that the majority of the supplied electrical power (~mW) goes to maintaining the plasmonic excitation, with only a small fraction (~μW) being converted into emitted THz radiation. Output power could, in principal, be increased by fabricating devices comprising a common gate, which is positioned close to a series of parallel conducting channels rather than just a single conducting channel. An example of this is shown in Figure 9, where we have fabricated multiple parallel conducting channels by removing InGaAs material in the regions labeled “Etched” in the lower image. The upper scanning electron microscope (SEM) image shows parallel conducting channels formed in an InGaAs quantum well by selective etching. Large squares to the left and right are pad areas for subsequent fabrication of gate contacts. The lower image in Figure 9 shows an expanded view of the area enclosed by the white dotted line in the upper image. This shows in clearer detail the high aspect ratio of the etching procedure used to define parallel conducting channels. However, a similar approach in which the 2DEG is replaced by graphene offers some potential advantages.

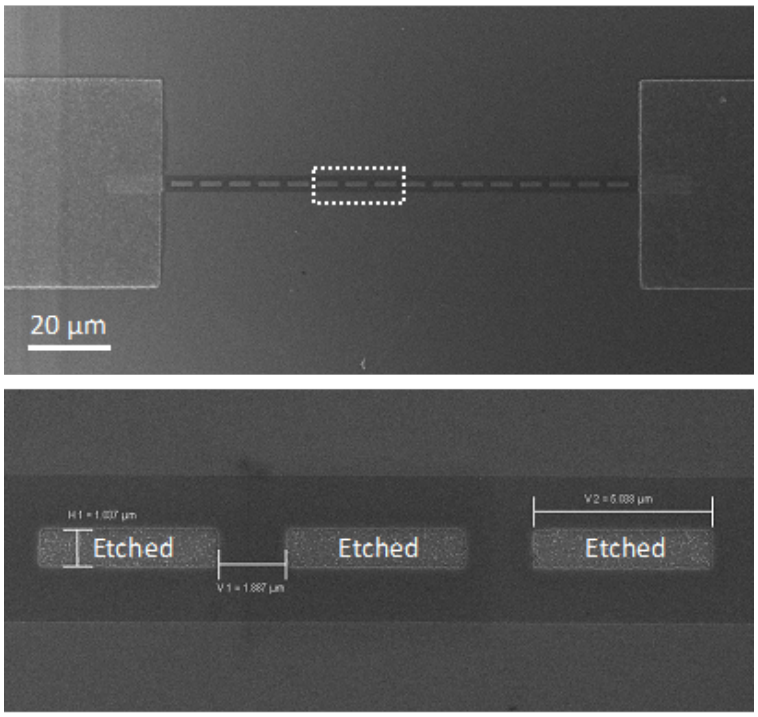

Figure 9. Electron Micrographs of THz Source Device Fabricated with Parallel Conducting Channels

4.1.1 Graphene-based THz Source. After demonstrating signatures of plasma-wave excitation in III–V semiconductor high-mobility transistors (discussed in Section 4.0), we moved to implement the analogous device in a graphene-based system. Such devices are expected to exhibit advantages over their III–V based counterparts, most notably through their high mobility, the capacity to tune plasmonic resonances over wide frequency ranges, and the ease with which it is expected that such devices can be used to launch terahertz plasmons for on-chip terahertz communications.

The approach that we are pursuing involves the use of established transfer techniques to stack high-quality heterostructures of graphene and hexagonal boron nitride (h-BN) in predetermined multilayers. As a first step towards the fabrication of plasmonic transistors based upon this approach, we have been working to implement, in-house, a reliable procedure for the stacking of graphene and h-BN. An example of our progress is provided in Figure 10, which identifies two graphene flakes (outlined with white dotted lines in panel (a)) that were transferred to a large flake of h-BN on a dielectric SiO_2 substrate. The transferred graphene is not readily visible in panel (b) but is detected in panel (c) (in the enclosed rectangle) by means of Raman spectroscopy mapping. Colors in the overlaid Raman map indicate the intensity of the characteristic graphene 2D peak, located at 2700 cm^{-1}, and the red regions correspond to the outlined graphene shown in panel (a). These results demonstrate promising progress towards the fabrication of the proposed graphene terahertz transistor.

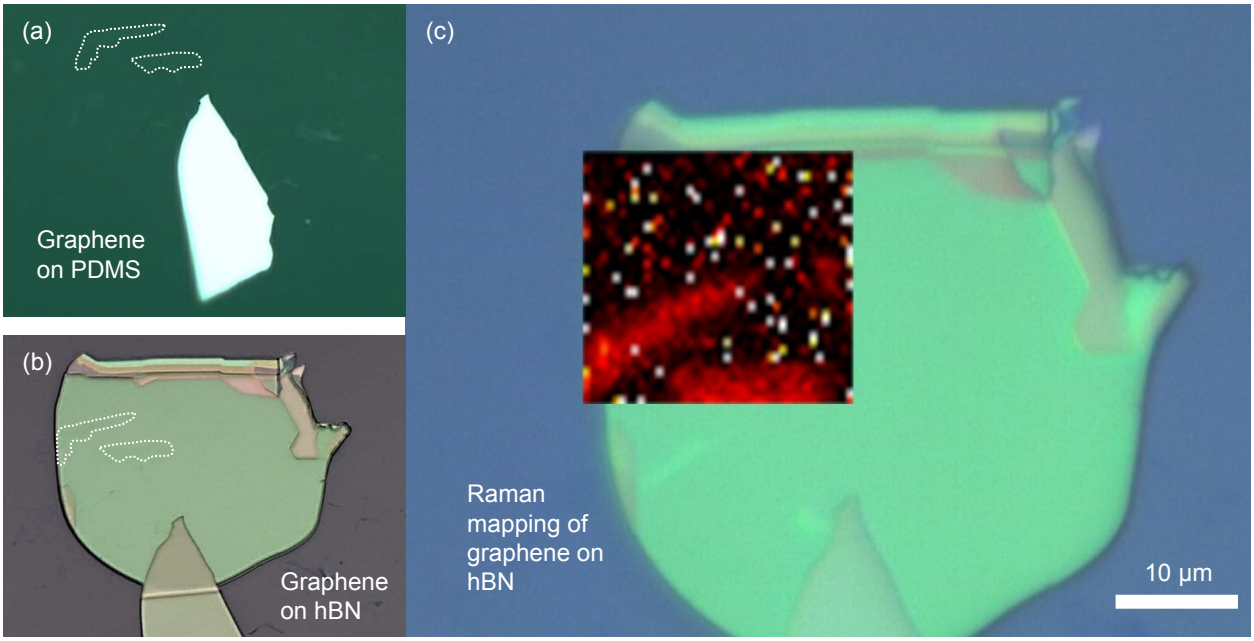

Figure 10. Optical Micrographs of Graphene Flakes Transferred onto Hexagonal Boron Nitride Confirmed by Raman Mapping

In the final stages of this program, we developed advanced cleanroom techniques for the fabrication of plasmonic transistors based on the graphene-on-hBN system. This work included refining the oxygen-plasma etching conditions to form graphene layers with well-defined probe geometries for contact deposition, and deposition of metal electrodes by advanced lift-off. Having implemented these strategies, by the conclusion of this research we were at the point of being able to fabricate devices reproducibly with desired tolerance. This positions us well to explore the electrical and optical characteristics in future research.

4.2 Graphene–Metal Hybrid Array

Our earlier results (Figure 2) showed that having a continuous graphene film surrounding metal patch antennas resulted in reduced reflection from the array. We therefore conceived a reflectarray design in which graphene acts only as a small tuning element within a metallic element. The concept behind this design is to use metallic patches to determine the resonant frequency and to ensure good reflectivity of the incoming signal. We attach to the metal patch a small (µm size) rectangular graphene stub to provide the appropriate phase shift by acting as a plasmonic stub to the metallic patch antenna. Figure 11a shows incident and reflected SPP waves in the graphene stub [41]. The basic representation of an element of a reflectarray with metal patch graphene stub is shown in Figure 11b. Figure 11c shows a working concept of the graphene stub based reflectarray with rows and columns of multiple elements made up of patch and stub. The calculated relative phase delay as a function of the Fermi energy in the graphene stub [42] is shown in Figure 11d.

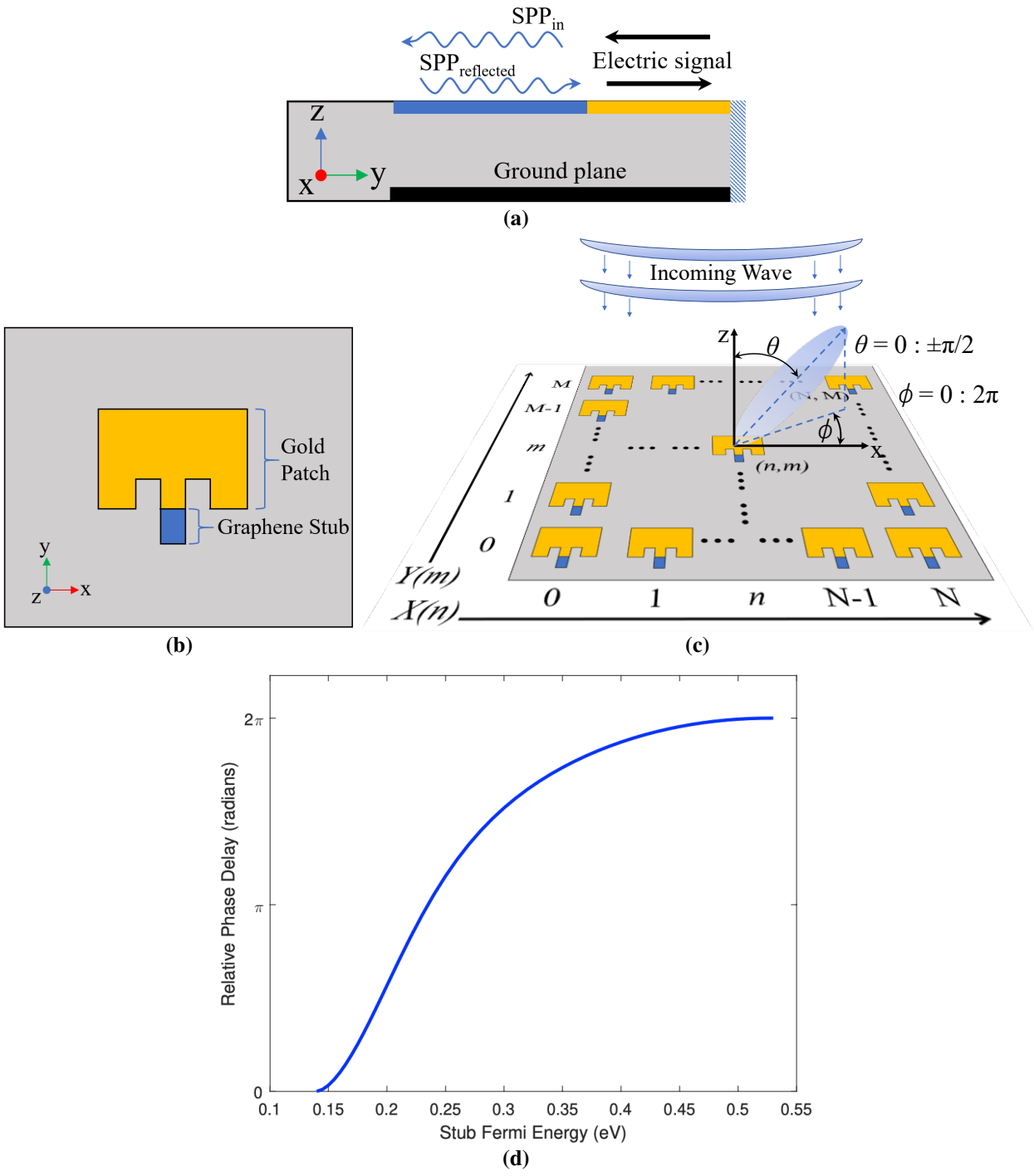

Figure 11. Active Reflectarray Concept using Metallic Patch and Graphene Stub

4.2.1 Graphene Stub Design. The phase delay mechanism of the concept shown in Figure 11 works on the principle of transmission lines, where the electric signal in the metal patch is transmitted along the stub as an SPP wave, which propagates along the length of a stub and is reflected back from the stub–dielectric boundary. In a conventional design, having an arrangement of patch antenna elements where the physical stub lengths vary would result in different propagation times for the SPP wave, thus a phase delay in the reflected signal. The required degree of control over the phase delay determines the variation in the lengths of the stubs and their repetition. For graphene plasmonic waveguides, it has been shown that despite keeping the physical length of different graphene structures the same, the *effective* SPP propagation length can be changed by changing the Fermi energy [43]. For the same scattering time and temperature, two graphene stubs at different Fermi energies show different effective SPP propagation lengths (due to different SPP propagation speed). Consequently, a phase shift could be introduced by adjusting the Fermi level in the graphene stub even if all the stubs had the same physical length. Singh et al. calculated that for an E_F value of 0.13 eV, the effective graphene length corresponds to one and a half SPP wavelength, introducing a phase change of π whereas for an E_F value of 0.28 eV, the effective graphene length corresponds to one full SPP wavelength causing a 2π phase change. Figure 11d shows the calculated values of the relative phase delays between the graphene stubs as a function of their Fermi energy [41], suggesting that the 0 to 2π phase range necessary for total spatial profiling could be achieved by a modest tuning of graphene's Fermi energy between 0.15 and 0.5 eV. The result is a continuously tunable reflectarray, or IRS.

At room temperature and without any external biasing/doping mechanism, graphene behaves like a weak metal where its Fermi energy is on the order of a few meV and the mobility is a few thousand $\mathrm{cm^2\,V^{-1}\,s^{-1}}$. While this might be sufficiently conducting to cross the metal–stub boundary, the SPP must survive the round-trip along the stub without being damped or dephased due to scattering. After several failed attempts, THz–TDS characterization revealed that the "graphene only stub" design shown in Figure 11 is very difficult to achieve using CVD-grown graphene because the momentum relaxation time of the charge carriers (< 100 fs) is considerably shorter than initially assumed (500 fs). This realization led to a modification of our hybrid IRS design.

4.2.2 Graphene Gap Design. Although graphene cannot sustain the THz plasmons in the entirety of the stub length, it remains an attractive material due to the fact that its Fermi energy can be tuned by various methods [44, 45]. To enable tunability of the stub while minimizing losses, we designed an IRS where the patch and stub both are made of metal but the stubs are "broken" leaving a small gap. This gap acts as a dielectric between two conductors. If the stub lengths of all the elements in the array are the same, as shown in Figure 12a, there should be no phase change in the re-radiated signal, (i.e., the reflected signal should be specular). If the gaps are filled, patch antennas with stubs of different physical length (Figure 12b) steer the reflected signal, resulting in non-specular reflection. In our design, the gaps are bridged by graphene (Figure 12c), which has

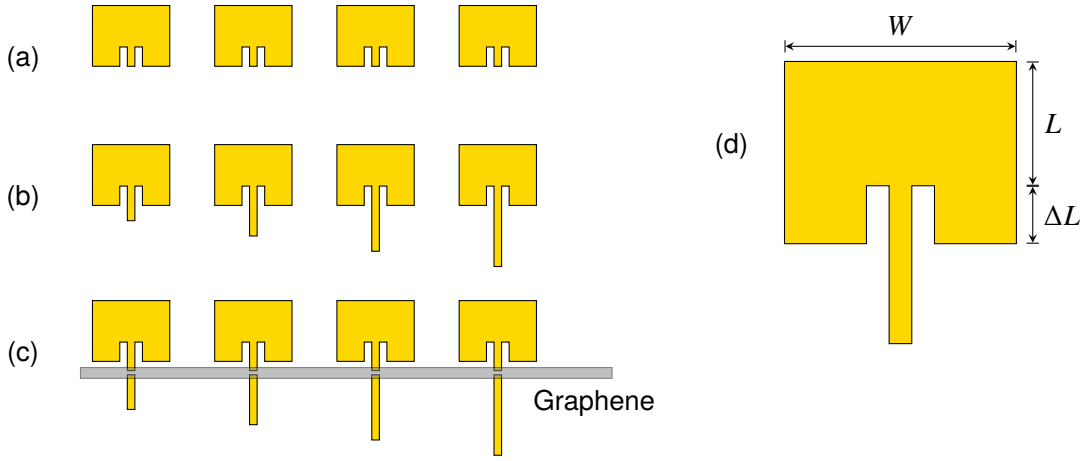

Figure 12. Graphene–Gap Active Reflectarray Design

tunable conductivity. Hence, by adjusting the Fermi level in this gap, the stub can be electrically broken or continuous. The result is a graphene–metal hybrid IRS where the resonance frequency is determined by the metal patch size and the phase shift is governed by the tunable graphene element. Under the effects of an externally applied electric bias, the change in the Fermi energy and thus in the gap conductivity should be enough to sustain the signal and allow it to travel from one metal–graphene boundary in the stub to the other. This provides a kind of electrical switch, connecting stubs of different lengths for the signal to traverse and hence, switchable phase difference in the re-radiated signal.

4.3 IRS Design Verification

Before introducing graphene into the stub gaps, we need to establish that our designed structure indeed works at the desired resonance frequency. This can be done by fabricating a metal-only reflectarray where the phase delay provided by the stubs is fixed (i.e., different lengths, no gaps). Patch dimensions considered during the antenna design are shown in Figure 12d. In our initial design, all the parameters were calculated such that the resonance frequency would be 1.25 THz, as this corresponds to the peak sensitivity of our THz–TDS system. The upper portion of Figure 13 shows a reflectance spectrum of two reflectarrays, one with no phase delay (uniform stub length) and one with a fixed phase delay, using doped Si as the ground plane. The array dimensions are 2 mm × 2 mm, and vertical red lines correspond to the water vapor absorption peaks. The non-specular reflection for the fixed phase delay should direct the component of the THz pulse near the resonance frequency away from the detector, resulting in a clear dip in reflectance. No feature is seen near 1.25 THz for either design.

A side view of the designed structure is shown to the right, in which a dielectric material with a total thickness in excess of 2.0 µm separates the reflectarray from the doped Si wafer that acts as the ground plane. The reason for the failure of these structures is the fact that the doped Si wafer used

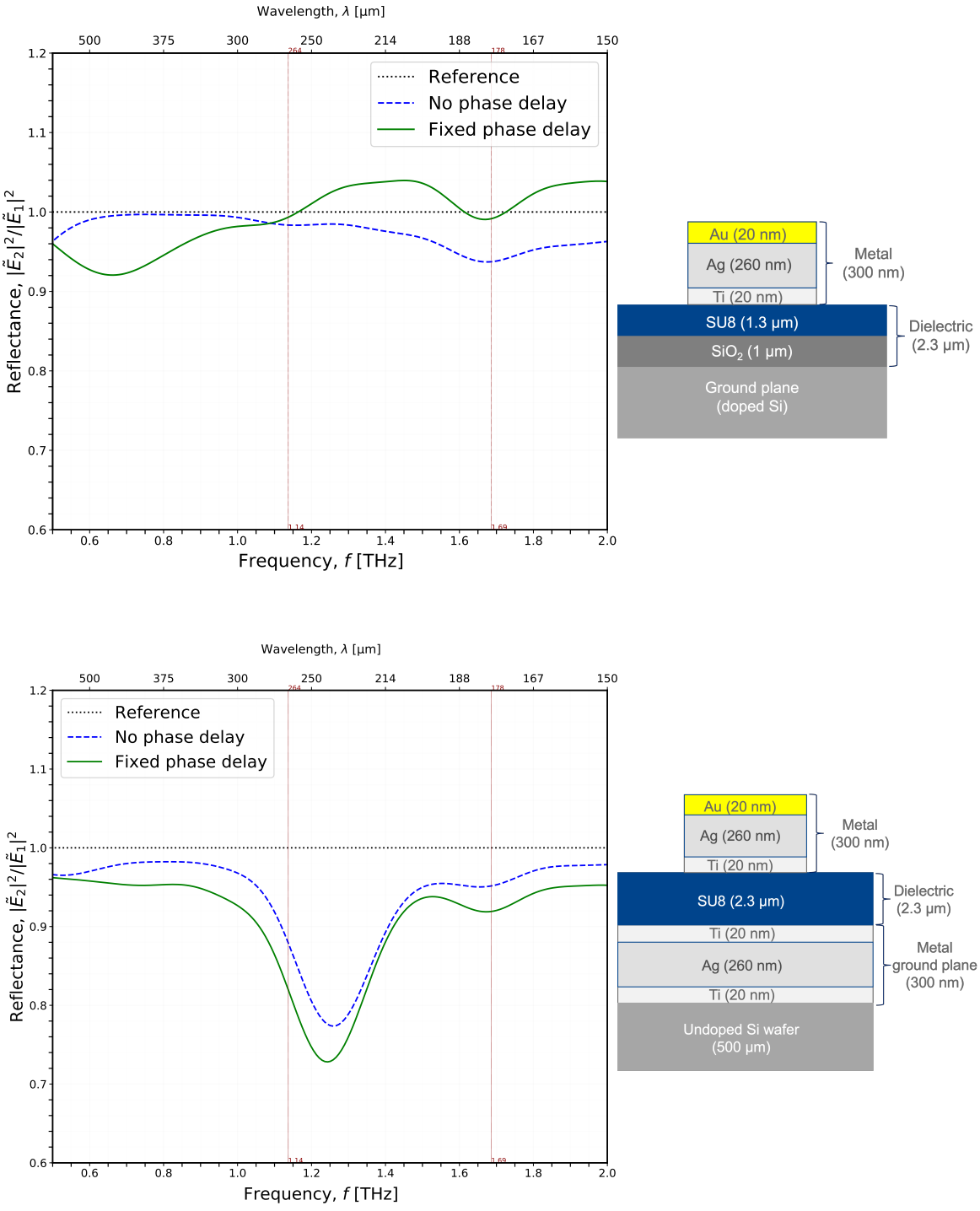

Figure 13. Reflectance Measurements of Reflectarrays Designed for 1.25 THz Response

as the substrate was not sufficiently conducting to act as a ground plane. In the absence of a ground plane, the reflectarray antenna becomes ineffective and the reflection provided by the structure is purely specular. To resolve this issue, we coated the Si substrate with a 300 nm metal layer, and then fabricated the rest of the structure atop this well-defined ground plane. In the absence of SiO_2, we increased the spin-coated SU8 dielectric thickness to 2.3 μm (Figure 13, lower right). It can be seen in the lower spectra in Figure 13 that with the introduction of a metallic ground plane clearly shows the expected dip in reflection. The full width at half-maximum (FWHM) of the reflection dip is approximately 0.25 THz whereas at ~1.25 THz more than 25% drop in the reflection (as compared to the reference sample) can be observed. This indicates that the fabricated structure is deflecting the resonant frequency away from the detector due to the phase delay provided by the stubs and acts like a normal metal reflector for all other frequencies. Due to the fixed setup of emitter and detector in our THz system, it is hard to verify the angle at which the resonant frequency is being reflected by the structure. Moreover, we also see a dip for the fixed phase delay structure, meaning a non-specular reflection measurement is necessary to confirm the dip is actually due to a steered beam rather than absorption, scattering, or other losses. Nonetheless, the clear dip in reflectance at the design frequency gives strong indication that the fabricated structure provides the desired phase delay and thus shows beamforming capabilities, albeit at a fixed angle.

4.3.1 IRS Redesign for 1.0 THz. To verify the reflectarray operation, we redesigned the array structure to work at 1.0 THz. In addition to a 2 mm × 2 mm array, we also made a larger 12.5 mm × 12.5 mm reflectarray for measurement using the *TeraNova* platform (described in section 4.4). The steps described previously for the fabrication of the small 2 mm × 2 mm reflectarray are repeated for the fabrication of the large array using the "fixed phase delay" design on the photomask. For the reference sample, all the fabrication steps are the same until the dielectric deposition, but no array structures are fabricated. Another reference sample was fabricated in which a continuous 300 nm metal film was deposited on top of the dielectric layer to verify that the designed metallic reflectarray behaves differently than a continuous metal film. A photograph and an optical micrograph of IRS designed for 1.0 THz are shown in Figure 14 (a) and (b), respectively.

Figure 15a shows reflectance spectra for the redesigned 1.0 THz structures (fixed phase delay) with respect to (a) a continuous metal film and (b) rotation of the array (perpendicular to incident polarization). Spectra are normalized relative to the dielectric-coated substrate. As expected, the continuous metal film shows slightly higher reflectance than the reflectarray, and has no prominent features. A drop in reflectance can be clearly seen near 0.9 THz. Figure 15b shows the reflectance spectrum for the aligned and rotated array. The peak near 1.0 THz disappears, suggesting the array is behaving as expected. The mismatch with the design frequency is because the length and width were swapped at some point during the photomask design process. However, the FWHM value of the dip is approximately 0.2 THz and the total drop in reflection is nearly 25%, thus there should still be a measurable effect at 1.0 THz.

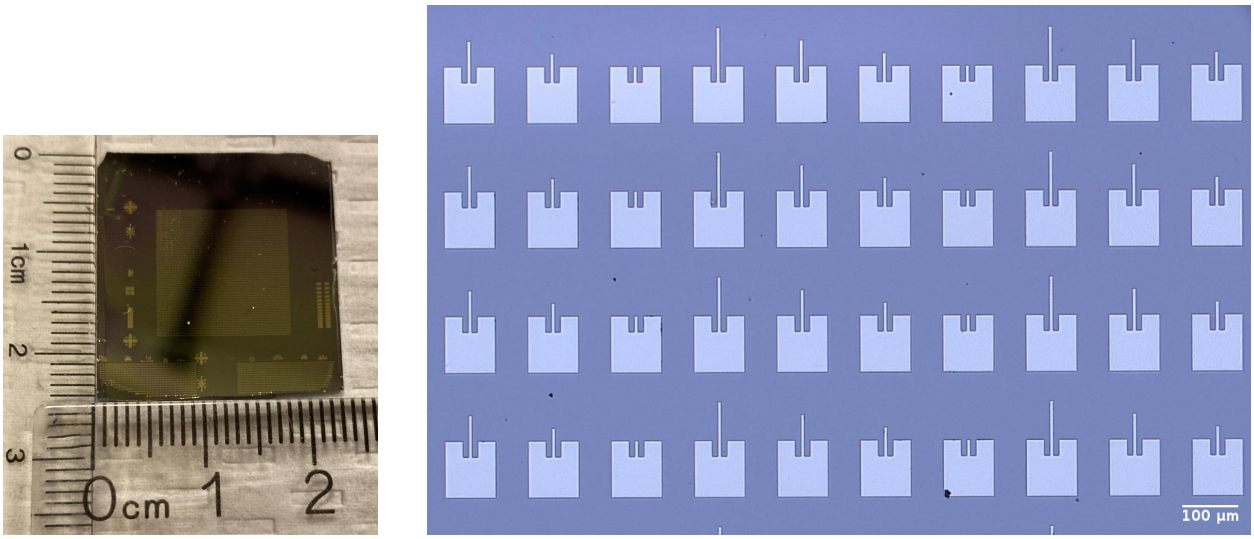

(a) (b)

Figure 14. Optical Images of Reflectarray Designed for 1.0 THz

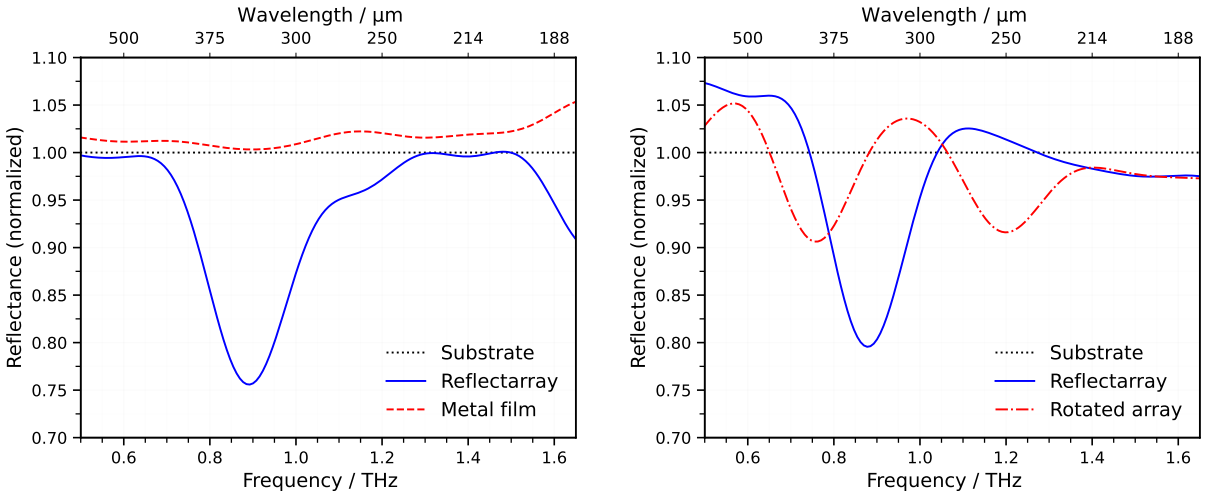

(a) **(b)**

Figure 15. Reflectance Measurements of Reflectarrays Designed for 1.0 THz Response

4.4 Demonstration of IRS Beamsteering

From the THz reflection measurements shown in Figure 15, we can conclude that the IRS is showing resonance at the expected frequency by steering the beam away from the THz detector, but we cannot confirm that the beam is being deflected at the expected angle (22.5° from the normal). We verified non-specular reflection of the fabricated array using the *TeraNova* testbed, which consists of two nodes. In transmission, a Schottky-diode-based frequency multiplier (Virginia Diodes, Inc.) is used to generate a THz carrier signal in the first absorption-defined transmission window above 1 THz, i.e., between 1 and 1.075 THz, starting from a local oscillator (LO) at 41 to 44 GHz provided by a Keysight PSG E8257. A sub-harmonic mixer based on the same technology is then used to modulate the THz carrier signal with the information signal to be transmitted, generated by means of a broadband arbitrary waveform generator (Keysight AWG M8196A), which has an analog bandwidth of 32 GHz per channel and a sampling rate of up to 92 Giga-Samples-per-second (GSas) with 8-bit resolution. Each waveform can be defined with up to 512 kSa, allowing precise control of baseband signals. In reception, the same setup is used to down-convert the modulated THz signal and recover the transmitted symbols. The downconverted signals are digitally stored prior to signal processing via a high-performance digital oscilloscope (Keysight DSO Z632A), which has up to 63 GHz of real-time analog bandwidth. This equipment allows us to conduct time-domain measurements with very high resolution, which can then be post-processed. Directional horn antennas with 30 dBi gain are used in transmission and reception.

A sinusoidal signal of frequency 1 GHz is generated using the Keysight arbitrary waveform generator and sent in intermediate frequency (IF) to the transmitter/upconverter frontend which upconverts the IF signal to a center frequency of 1 THz by mixing it with a 1 THz signal which is generated by passing a 41.67 GHz LO carrier signal (generated by the Keysight PSG) through a (×24) frequency multiplier chain. The upconverted signal is then sent over the air to the reflectarray at normal/perpendicular incidence ($\theta = 0°$) via the 30 dBi high-gain directional horn antenna. A schematic of the experimental setup and photos of the the transmitter, receiver, and non-specular measurement geometry of the reflectarray ($\theta \approx 22.5°$) are depicted in Figure 16. The reflectarray then intercepts the incoming signal at 0°, steers and reflects it controllably at 22.5°. The receiver/downconverter frontend is placed at exactly 22.5° and intercepts the reflected signal via the same directional high gain horn antenna, the received signal is then amplified using a high performance low-noise amplifier (LNA), downconverted back to IF, filtered and stored using the high-performance digital oscilloscope for further signal processing. A metal sheet is placed in the same position of the reflectarray to demonstrate the controlled reflection capabilities of the fabricated reflectarray. The received IF signal is processed and its frequency spectrum is obtained to demonstrate that the transmitted IF tone at 1 GHz was only detectable in the case of the reflectarray, indicated by the red circle in Figure 17. Only noise was received (i.e., no controlled reflection) when the reflecting surface was a metal sheet (Figure 18), as expected for specular reflection.

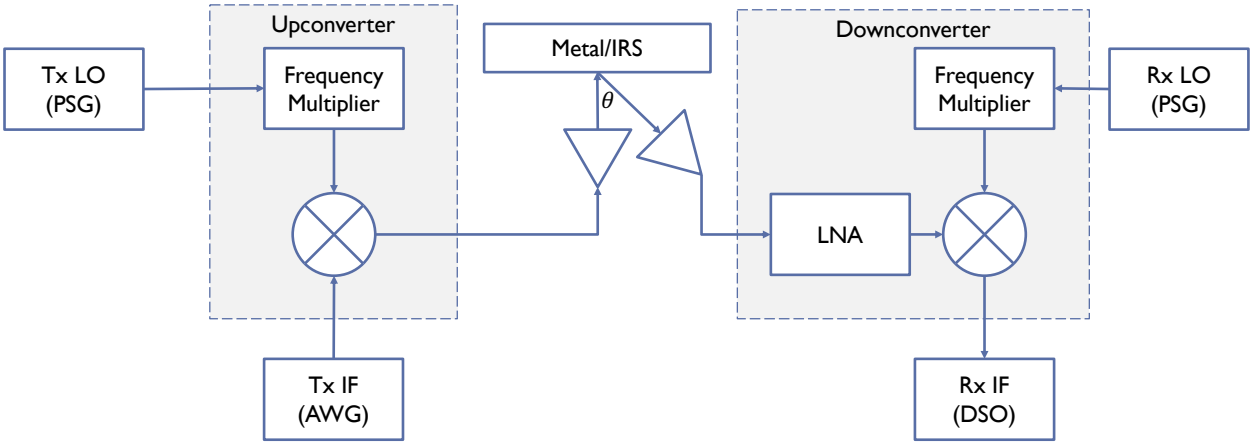

(a)

Transmitter

Receiver

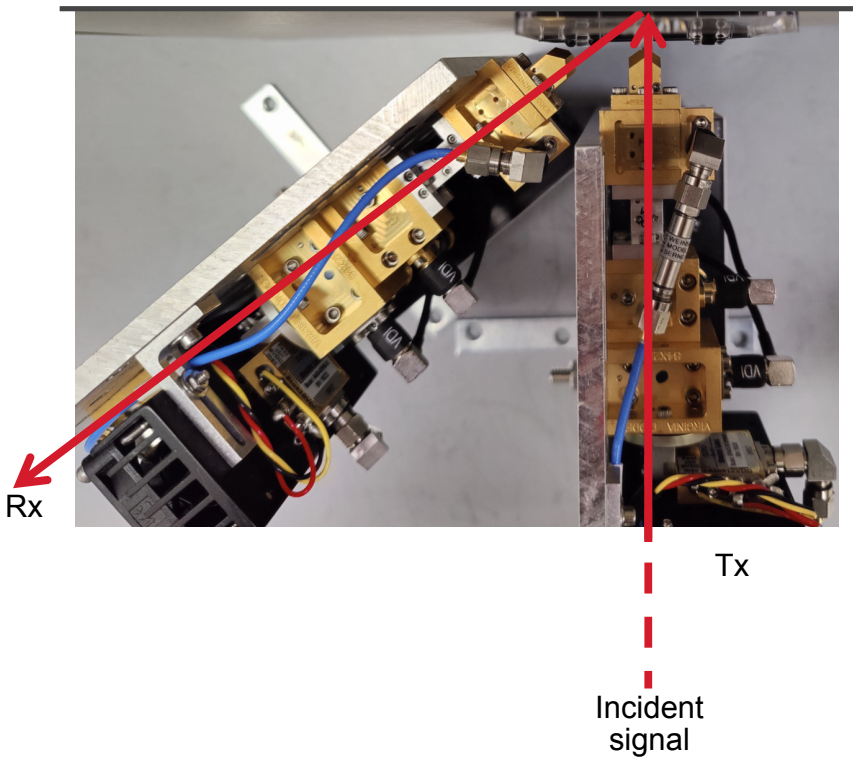

(b)

Figure 16. TeraNova Testbed Schematic, Components, and Non-Specular Measurement Configuration

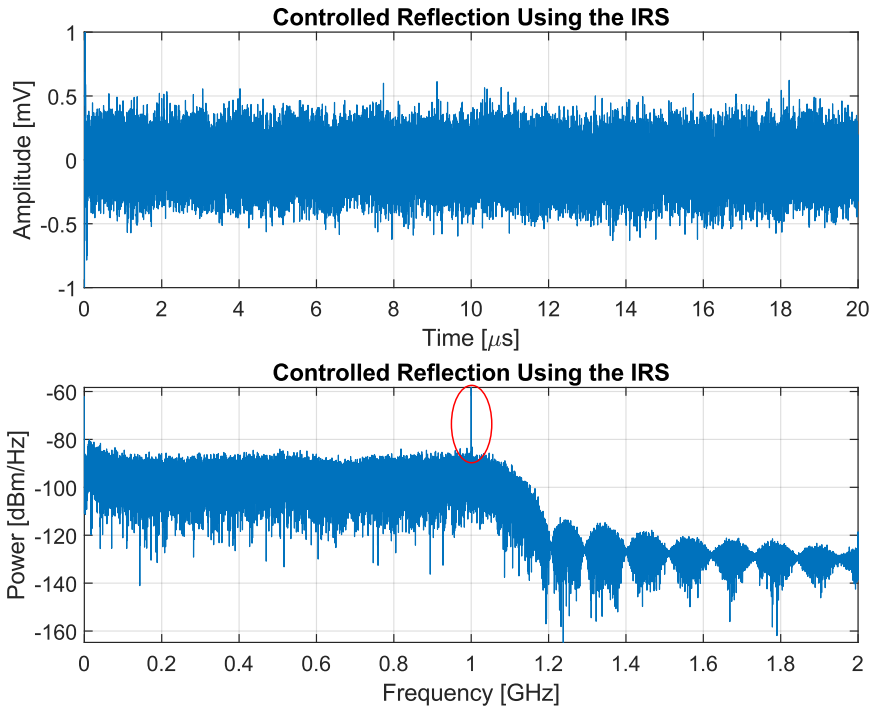

Figure 17. Time-Domain Signal and Corresponding Frequency Spectrum of the Reflectarray

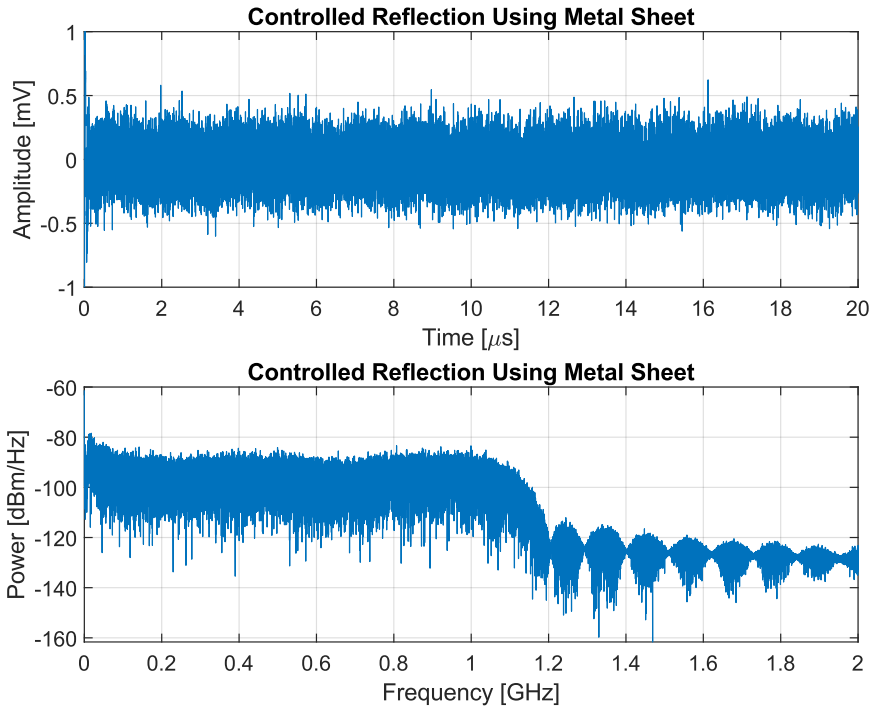

Figure 18. Time-Domain Signal and Corresponding Frequency Spectrum of a Metal Sheet

5.0 CONCLUSIONS

The objective of the proposed research was to develop, design, and fabricate two types of active antenna arrays for the terahertz (THz) band, the first being a graphene/metal hybrid reflect array and the second a transmit array integrated with an on-chip, electronically driven plasmonic THz source. The targeted breakthrough was to demonstrate active array control and, thus, beamforming, in both transmission and reflection, at or above 1 THz. The results of this project are two successes and two shortcomings—one each for the THz source and array.

On the THz source topic, we were unable to directly detect THz frequency emission from the device. However, we were successful in developing a robust understanding of the underlying physics, which taught us that joule heating is the dominant power dissipation mechanism, thus radiated power should be weak. We showed that fabricating multiple plasmonic cavities in parallel is feasible and should improve the radiated power, facilitating direct detection. We also performed thorough electrical characterization of our plasmonic devices, which matched numerical models developed in collaboration with our colleagues. This provided very strong evidence of an electrically driven THz frequency plasmonic transistor, and enabled us to rule out any alternative explanations for our experimental observations. We published these findings in *Nano Letters* [40].

On the reflectarray topic, we did not get to the point of demonstrating active control, but we introduced two graphene-based active reflectarray designs. One design offers full beamsteering capabilities but requires high-quality graphene that is difficult to obtain on square-centimeter scales using existing growth and transfer techniques. The second design can use conventional CVD-grown graphene but offers limited beamsteering capabilities. We fabricated reflectarrays based on this second design and demonstrated a clear response near the design frequencies of 1.25 and 1.0 THz. In addition to solving several problems related to the design and fabrication of these arrays—such as dedicated ground-plane deposition and adhesion of the dielectric layer—we were successful in performing the first demonstration of non-specular reflection at 1.0 THz using a communications testbed at the AFRL Tech Showcase and Exchange Meeting in August, 2022. A peer-reviewed manuscript reporting these results is in preparation.

The work performed in this project leveraged a state-of-the-start experimental platform for communication and networking at true THz frequencies funded by the National Science Foundation (NSF), as well as the team's prior results supported by AFOSR award FA9550-16-1-0188 and Air Force Research Laboratory (AFRL) award FA8750-15-1-0050. Our findings also suggest two promising future directions, both of which would leverage the 2D material system graphene-on-hBN. It is known that the charge-carrier mobility in graphene is significantly improved when supported by hBN, thus making it more suitable for the fabrication of plasmonic transistors than the III–V semiconductors used in this project. The increased mobility would also address challenges related to scattering of the SPP wave that faced in the active reflectarray design.

6.0 REFERENCES

[1] Akyildiz, I. F., Jornet, J. M., and Han, C., "Terahertz band: Next frontier for wireless communications," *Physical Communication*, **12**, 2014, pp. 16–32.

[2] Kurner, T. and Priebe, S., "Towards THz Communications-Status in Research, Standardization and Regulation," *Journal of Infrared, Millimeter, and Terahertz Waves*, **35**, 2014, pp. 53–62.

[3] Dyakonov, M. and Shur, M., "Shallow water analogy for a ballistic field effect transistor: New mechanism of plasma wave generation by dc current," *Physical Review Letters*, **71**, 1993, p. 2465.

[4] Nafari, M., Aizin, G. R., and Jornet, J. M., "Plasmonic HEMT Terahertz Transmitter based on the Dyakonov-Shur Instability: Performance Analysis and Impact of Nonideal Boundaries," *Phys. Rev. Applied*, **10**, 2018, p. 064025.

[5] Chen, R. et al., "High-Voltage Breakdown and the Gunn Effect in GaAs/AlGaAs Nanoconstrictions," *IEEE Transactions on Nanotechnology*, **14**, 2015, pp. 524–530.

[6] Dyakonov, M. and Shur, M. S., "Current instability and plasma waves generation in ungated two-dimensional electron layers," *Applied Physics Letters*, **87**, 111501 2005, p. 111501.

[7] Nikpaik, A. et al., "A 219-to-231 GHz Frequency-Multiplier-Based VCO With ~3% Peak DC-to-RF Efficiency in 65-nm CMOS," *IEEE Journal of Solid-State Circuits*, **53**, 2018, pp. 389–403.

[8] Aghasi, H., Cathelin, A., and Afshari, E., "A 0.92-THz SiGe Power Radiator Based on a Nonlinear Theory for Harmonic Generation," *IEEE Journal of Solid-State Circuits*, **52**, 2017, pp. 406–422.

[9] Deal, W. R. et al., "A 660 GHz up-converter for THz communications". *Compound Semiconductor Integrated Circuit Symposium (CSICS), 2017 IEEE*. IEEE. 2017, pp. 1–4.

[10] Leuther, A. et al., "20 nm Metamorphic HEMT technology for terahertz monolithic integrated circuits". *9th IEEE European Microwave Integrated Circuit Conference (EuMIC)*. IEEE. 2014, pp. 84–87.

[11] Urteaga, M. et al., "InP HBT technologies for THz integrated circuits," *Proceedings of the IEEE*, **105**, 2017, pp. 1051–1067.

[12] Mehdi, I. et al., "THz Diode Technology: Status, Prospects, and Applications," *Proceedings of the IEEE*, **105**, 2017, pp. 990–1007.

[13] Song, H.-J. et al., "Uni-travelling-carrier photodiode module generating 300 GHz power greater than 1 mW," *IEEE Microwave and Wireless Components Letters*, **22**, 2012, pp. 363–365.

[14] Huang, S.-W. et al., "Globally stable microresonator Turing pattern formation for coherent high-power THz radiation on-chip," *Physical Review X*, **7**, 2017, p. 041002.

[15] Nagatsuma, T., Ducournau, G., and Renaud, C. C., "Advances in terahertz communications accelerated by photonics," *Nature Photonics*, **10**, 2016, p. 371.

[16] Lu, Q. et al., "Room temperature continuous wave, monolithic tunable THz sources based on highly efficient mid-infrared quantum cascade lasers," *Scientific Reports*, **6**, 2016.

[17] Ferrari, A. C. et al., "Science and technology roadmap for graphene, related two-dimensional crystals, and hybrid systems," *Nanoscale*, **7**, 2015, pp. 4598–4810.

[18] Ju, L. et al., "Graphene plasmonics for tunable terahertz metamaterials," *Nature Nanotechnology*, **6**, 2011, pp. 630–634.

[19] Schwierz, F., "Graphene transistors," *Nature Nanotechnology*, **5**, 2010, p. 487.

[20] Wu, Y. et al., "200 GHz Maximum Oscillation Frequency in CVD Graphene Radio Frequency Transistors," *ACS Applied Materials & Interfaces*, **8**, 2016, pp. 25645–25649.

[21] Karmakar, A. et al., "Experimental characterization of a hybrid graphene/metal plasmonic antenna array". *Proc. of the 5th ACM/IEEE International Conference on Nanoscale Computing and Communications (NanoCom)*. 2018.

[22] Fan, A., Rahman, A., and Reif, R., "Copper wafer bonding," *Electrochemical and Solid-State Letters*, **2**, 1999, p. 534.

[23] Kim, S. M. et al., "The effect of copper pre-cleaning on graphene synthesis," *Nanotechnology*, **24**, 2013, p. 365602.

[24] Hao, Y. et al., "The role of surface oxygen in the growth of large single-crystal graphene on copper," *Science*, **342**, 2013, pp. 720–723.

[25] Wofford, J. M. et al., "Graphene islands on Cu foils: the interplay between shape, orientation, and defects," *Nano Letters*, **10**, 2010, pp. 4890–4896.

[26] Trehan, Y., "The reduction of copper oxides by molecular hydrogen," *Zeitschrift für anorganische und allgemeine Chemie*, **318**, 1962, pp. 107–112.

[27] Vlassiouk, I. et al., "Role of hydrogen in chemical vapor deposition growth of large single-crystal graphene," *ACS Nano*, **5**, 2011, pp. 6069–6076.

[28] Yu, Q. et al., "Control and characterization of individual grains and grain boundaries in graphene grown by chemical vapour deposition," *Nature Materials*, **10**, 2011, pp. 443–449.

[29] Tsen, A. W. et al., "Tailoring electrical transport across grain boundaries in polycrystalline graphene," *Science*, **336**, 2012, pp. 1143–1146.

[30] Yan, Z., Peng, Z., and Tour, J. M., "Chemical vapor deposition of graphene single crystals," *Accounts of Chemical Research*, **47**, 2014, pp. 1327–1337.

[31] Yan, Z. et al., "Toward the synthesis of wafer-scale single-crystal graphene on copper foils," *ACS Nano*, **6**, 2012, pp. 9110–9117.

[32] Chen, S. et al., "Millimeter-size single-crystal graphene by suppressing evaporative loss of Cu during low pressure chemical vapor deposition," *Advanced Materials*, **25**, 2013, pp. 2062–2065.

[33] Kashyap, P. K., Sharma, I., and Gupta, B. K., "Continuous growth of highly reproducible single-layer graphene deposition on Cu foil by indigenously developed LPCVD setup," *ACS Omega*, **4**, 2019, pp. 2893–2901.

[34] Li, X. et al., "Transfer of large-area graphene films for high-performance transparent conductive electrodes," *Nano Letters*, **9**, 2009, pp. 4359–4363.

[35] Barin, G. B. et al., "Optimized graphene transfer: Influence of polymethylmethacrylate (PMMA) layer concentration and baking time on graphene final performance," *Carbon*, **84**, 2015, pp. 82–90.

[36] Karmakar, A. et al., "Approaching completely continuous centimeter-scale graphene by copolymer-assisted transfer," *RSC Advances*, **8**, 2018, pp. 1725–1729.

[37] Abohmra, A. et al., "Terahertz antenna array based on a hybrid perovskite structure," *IEEE Open Journal of Antennas and Propagation*, **1**, 2020, pp. 464–471.

[38] Sen, P. et al., "The TeraNova platform: An integrated testbed for ultra-broadband wireless communications at true Terahertz frequencies," *Computer Networks*, **179**, 2020, p. 107370.

[39] Sugaya, T. et al., "Quantum-interference characteristics of a 25 nm trench-type InGaAs/InAlAs quantum-wire field-effect transistor," *Applied Physics Letters*, **80**, 2002, pp. 434–436.

[40] Barut, B. et al., "Asymmetrically Engineered Nanoscale Transistors for On-Demand Sourcing of Terahertz Plasmons," *Nano Letters*, **22**, 2022. PMID: 35312324, pp. 2674–2681.

[41] Singh, A. et al., "A hybrid intelligent reflecting surface with graphene-based control elements for THz communications". *2020 IEEE 21st International Workshop on Signal Processing Advances in Wireless Communications (SPAWC)*. IEEE. 2020, pp. 1–5.

[42] Singh, A. et al., "Design and Operation of a Smart Graphene–Metal Hybrid Reflectarray at THz Frequencies". *2020 14th European Conference on Antennas and Propagation (EuCAP)*. 2020, pp. 1–5.

[43] Singh, P. K. et al., "Graphene-based plasmonic phase modulator for terahertz-band communication". *2016 10th European Conference on Antennas and Propagation (EuCAP)*. IEEE. 2016, pp. 1–5.

[44] Sensale-Rodriguez, B. et al., "Unique prospects for graphene-based terahertz modulators," *Applied Physics Letters*, **99**, 2011, p. 113104.

[45] Sensale-Rodriguez, B. et al., "Broadband graphene terahertz modulators enabled by intraband transitions," *Nature Communications*, **3**, 2012, pp. 780+.

LIST OF SYMBOLS, ABBREVIATIONS, AND ACRONYMS

2DEG	two-dimensional electron gas
AFOSR	Air Force Office of Scientific Research
AFRL	Air Force Research Laboratory
CMOS	complementary metal-oxide semiconductor
CVD	chemical vapor deposition
DI	deionized
FET	field-effect transistor
FWHM	full width at half-maximum
h-BN	hexagonal boron nitride
HBT	heterojunction bipolar transistor
HEMT	high electron-mobility transistor
ICP-RIE	inductive coupled plasma-reactive ion etching
IF	intermediate frequency
IPA	isopropyl alcohol
IRS	intelligent reflecting surface
LNA	low-noise amplifier
LO	local oscillator
NDC	negative differential conductance
NSF	National Science Foundation
PMMA	polymethylmethacrylate
PVD	physical vapor deposition
QCL	quantum cascade laser
RIE	reactive ion etching
SEM	scanning electron microscope
SPP	surface plasmon polariton
THz	terahertz
THz–TDS	terahertz time-domain spectroscopy